Arctic Cloud–Radiation–Temperature Associations in Observational Data and Atmospheric Reanalyses

JOHN E. WALSH AND WILLIAM L. CHAPMAN

Department of Atmospheric Sciences, University of Illinois, Urbana–Champaign, Illinois

(Manuscript received 18 September 1997, in final form 26 January 1998)

ABSTRACT

Associations between cloudiness, radiative fluxes, and surface air temperature in the central Arctic are evaluated from 1) measurements made at Russian drifting ice stations, and 2) atmospheric reanalyses of the National Centers for Environmental Prediction (NCEP) and the European Centre for Medium-Range Weather Forecasts (ECMWF). In the ice station data, cloudiness is associated with an increase of downward longwave radiation in all months and an increase of net (downward minus upward) total radiation from September through March. The surface air temperatures under overcast skies are 6°–9°C higher than under clear skies during September–March, and the differences are even larger when the observations are stratified by wind as well as cloudiness. The warming by the radiative flux enhancement after a transition from clear skies to overcast has a 1–2-day timescale, while the cooling after the transition to clear skies has a somewhat shorter timescale. The NCEP reanalysis exaggerates slightly the association between cloudiness and surface air temperature, while the ECMWF reanalysis shows a considerably weaker association.

The maximum cloud-radiative forcing (MCRF), defined as the difference between the ice station measurements of net surface radiation under cloudy and clear skies, ranges from -59 W m^{-2} in June to positive values of 20–30 W m^{-2} in September–March. The annual mean is small but positive, 3 W m^{-2}, despite the approximately three-month summer period of substantially negative MCRF. These findings are consistent with the conventional cloud-radiative forcing obtained in earlier studies using satellite data and one-dimensional models of the Arctic atmosphere and sea ice. Neither reanalysis captures the seasonality of the observationally deduced effects of clouds on surface radiation. The NCEP reanalysis does not capture the seasonality of the actual cloudiness (as defined by the reported cloud fractions), while the ECMWF reanalysis does not show an impact of clouds on the surface solar flux.

Issues needing further attention in the model–data comparison are the effects of surface heterogeneities, the characterization of Arctic clouds, the formulational reasons for the discrepancies between the model-derived reanalyses and the observational data, and the implications for model-derived projections of climate change in the Arctic.

1. Introduction

The polar regions are receiving increased scrutiny in climate change scenarios obtained from general circulation models. Much of this scrutiny arises from the polar amplification of the models' near-surface warming in simulations with increased concentrations of greenhouse gases. In many cases, the zonally averaged warming in the Arctic is two or three times larger than the global mean warning of 1.5°–4.5°C for a doubling of CO_2 (Manabe et al. 1992; IPCC 1996). The enhanced warming in high latitudes is at least partly attributable to the retreat of sea ice; this retreat is accelerated by the positive feedback between temperature and surface albedo. If the polar amplification of the warming as simulated by the climate models is a valid projection, then the ramifications for the permafrost and hydrology of the polar regions are substantial. However, the validity of the large polar amplification is confounded by several issues, one of which is the likelihood of associated changes in polar cloudiness. As in most other regions of the globe, clouds are the primary determinants of the variability of radiation that reaches the surface and drives the albedo–temperature feedback. Polar cloudiness and its characteristics can be expected to change considerably if a retreating sea ice cover creates larger areas of open (and warmer) water in the polar oceans. However, polar clouds are generally not well simulated by global climate models. Curry et al. (1996) survey the deficiencies in climate model simulations of polar cloud characteristics and cloud-radiative interactions, while Tao et al. (1996, their Fig. 8) show that even the cloud fractions vary tremendously among the global climate models used in the Atmospheric Model Intercomparison Project.

Ongoing Arctic field programs such as those of SHE-

Corresponding author address: Dr. John E. Walsh, Department of Atmospheric Sciences, University of Illinois, 105 S. Gregory Avenue, Urbana, IL 61801-3070.
E-mail: walsh@atmos.uiuc.edu

BA [Surface Heat Budget of the Arctic Ocean; cf. Perovich et al. (1997)], Department of Energy's Atmospheric Radiation Measurements (ARM)-North Slope of Alaska (Stamnes et al. 1999), and National Aeronautics and Space Administration's (NASA) FIRE-III (Randall et al. 1996) represent one prong of the effort to address deficiencies in model formulations of high-latitude processes involving polar clouds and radiative fluxes. This paper targets a similar objective by quantifying the polar cloud-temperature-radiative associations that must be captured by models if the polar climate simulations are to be considered realistic. For example, we will use existing data from Russian ice stations to evaluate the dependence of Arctic surface air temperatures and radiative fluxes on the concurrent cloud cover. This evaluation will complement Curry et al.'s (1993) one-dimensional model results and Schweiger and Key's (1994) satellite-derived radiative flux estimates, which show that the annual cycle of cloud-radiative forcing in the Arctic Ocean, unlike in lower latitudes, warms the surface at all times except during a portion of the summer when cloud-radiative cooling prevails. These associations can be crucial to valid simulations of Arctic climate changes such as those in the greenhouse scenarios.

The results obtained here from the observational data will be compared with corresponding evaluations from two recently released sets of atmospheric reanalysis products. While global climate models are the targets of the Arctic field programs noted above, the reanalysis products represent an attractive intermediate vehicle for assessment in this study because 1) the models used to assimilate data for the reanalyses are, in many respects, the same as the models used to simulate global climate, and 2) the observational constraints on the reanalyses can be expected to result in more realistic depictions of the primary atmospheric variables (wind, temperature, pressure) than is the case in unconstrained climate model simulations. Furthermore, in the absence of spinup problems, a reanalysis would be the ideal vehicle for testing model parameterizations, since the observational input can largely eliminate erroneous feedbacks on the large scale and thus enable the parameterization schemes to be driven by the ''best possible'' large-scale circulation. Even with modest spinup problems, the observational constraints and the generally higher resolution of the models used for the reanalyses create the potential for a more successful capture of cloud-temperature-radiative associations than in the ''unconstrained'' global climate models studied to date. The results in section 3 will show, however, that the reanalyses have a mixed record of success in this regard.

The data evaluation and reanalysis assessment will emphasize the associations between cloud coverage and surface air temperature, winds, sea level pressure, and the surface fluxes of shortwave (solar) and longwave radiation. The seasonal cycles of these associations will provide the means for assessing the associations, in the observational data and in the reanalyses, under the wide range of solar forcing that characterizes the polar climate. A notable limitation of this study is the use of cloud fraction as a measure of cloudiness. Cloud fraction in the Arctic is, in some respects, an elusive quantity because the inclusion of ''clear-sky'' ice crystals (''diamond dust'') can increase considerably the climatological estimates of wintertime cloud fractions (Curry and Ebert 1992, their Fig. 1). While information on optical depth (or even cloud base and thickness), phase (ice, liquid, mixed), ice or liquid water content, drop size, drop concentration, crystal habit, etc. would clearly be desirable for a diagnosis of the associations obtained here, the existing in situ data (and model output) do not permit the inclusion of these variables. In fact, a homogeneous database containing these variables is one of the primary objectives of the SHEBA–ARM–FIRE field programs (Randall et al. 1998).

In summary, this paper addresses two questions.

- How do surface radiative fluxes and temperatures depend on cloudiness and other variables through the seasonal cycle in the central Arctic?
- How well are the cloud-radiative-temperature associations captured by state-of-the-art atmospheric reanalyses?

The answer to the second question will have direct implications for the needs of the climate model counterparts of the global models used for the reanalyses, since unconstrained climate simulations should be no more successful than the data assimilations in capturing the cloud-radiative-temperature associations. In addition, some of the results obtained here will provide a base upon which the results of SHEBA–ARM–FIRE can build by including the important effects of surface heterogeneities. These effects are implicitly included in satellite-derived estimates of radiative fluxes and cloud-radiative effects, which will be an essential part of the scaling effort of SHEBA. Satellite-derived retrievals of radiative fluxes have been obtained for the Arctic, although the uncertainties and parameter sensitivities of the algorithms used to date are substantial (Schweiger and Key 1994; Key et al. 1997). We will cite the results of these studies in section 3.

2. Data and reanalysis products

a. The Russian ice station database

A series of drifting ice stations deployed by the former Soviet Union provided routine meteorological and other geophysical observations from the Arctic Ocean beginning in 1950 and continuing until 1991. The stations in this ''North Pole'' (NP) series were denoted sequentially as NP-2–NP-31. The time of occupation of each station ranged from several months to several years; the number of stations occupied at any specific time during the 1950–91 period was typically two or

three. The Arctic and Antarctic Research Institute (AARI) in St. Petersburg, former Soviet Union, archived the observations, which include the standard synoptic meteorological measurements (such as the air temperature, pressure, wind, and cloud fraction used in this study) as well as routine (four–eight times daily) measurements of surface radiative fluxes: downward solar (direct beam and diffuse), reflected solar, and net radiation (solar plus longwave). Marshunova and Mishin (1994) describe the radiative measurements and present a summary of monthly values. The standard meteorological measurements have been used in other recent studies (Martin and Munoz 1997; Serreze et al. 1997). The version of the dataset used here was provided on CD-ROM by the National Snow and Ice Data Center in Boulder, Colorado.

The accuracy of radiometric measurements in very cold evironments can be adversely affected by problems associated with calibration of the intruments and the need for maintenance, especially the frequent removal of frost from the instrument domes. The issue of instrumental accuracy is addressed by Marshunova and Mishin (1994, appendix A), who also note that the measured longwave and net total radiation data contain greater errors [''up to 30%,'' Marshunova and Mishin (1994, 2)] than do the measured solar fluxes. Maykut and Church (1973, 621), whose radiative measurements at Barrow, Alaska, were made during the middle portion (1962–66) of the NP ice station period, report that the estimated errors in their fluxes of solar, total incoming, and net total radiation were $\pm 6\%$.

Another important caveat concerning this study arises from the nature of the NP observations, which are point measurements from ice stations sited (for obvious logistical reasons) on relatively stable sea ice floes. Because thick first-year and multiyear ice floes generally provide the most stable ''platforms,'' one may assume that most of the measurements are representative of those surface types. Marshunova and Mishin (1994) state specifically that ''The radiation observation sites were chosen so that the sea-ice surface was characteristic of most of the floe and so that the sites would not be flooded during the summer snow melt.'' In reality, the pack ice of the Arctic Ocean is a heterogeneous mix of multiyear ice, first-year ice (thick in spring, when new stations were deployed), thin ice, open water or leads, and pressure ridges. The snow depth and, in summer, the stage of snowmelt can vary considerably not only among ice types but on the 10–100-m scale over a single ice type. While point measurements made over thick ice may be representative of larger areas in the case of some variables (e.g., atmospheric sea level pressure, wind), they will clearly not be representative in the case of other variables (upward longwave radiative flux, reflected solar radiation). Some small-scale variations of surface air temperature and the downward radiative fluxes can also be expected, although these variations should be much smaller than those of the upward radiative fluxes. We may also assume that the reported cloud fractions are, to a good approximation, the same as those that would have been reported from a different surface type within a distance of $\sim$10–100 km, which approaches the grid scale of an atmospheric model. One of the primary objectives of the SHEBA program is to address the representativeness of point measurements in regions of sea ice. In this respect, this study interfaces with SHEBA by providing a broader temporal perspective for the type of cloud-temperature-radiative associations that need SHEBA's spatial perspective and scaling.

b. Atmospheric reanalysis products

Atmospheric reanalyses provide a potentially useful bridge between point measurements (perhaps scaled to model grid cells via SHEBA or satellite algorithms) and the models used to simulate climate and climate change. The models used for the reanalyses are generally high-resolution counterparts of the models used in climate simulations. A reanalysis is performed by assimilating observational data into a numerical model at frequent intervals, for example, 6 h. The ''initial guess'' for the reanalysis at a particular time is the model's short-range (e.g., 6-h) forecast made from the time of the previous reanalysis. The output products of an atmospheric reanalysis include fields of the assimilation system's control variables such as wind, temperature, and pressure, as well as the model-computed fields of cloudiness, precipitation, and radiative fluxes. The latter fields will depend on the physical parameterizations used in the model and hence will be more uncertain than the fields of directly assimilated variables. Advantages of the reanalysis approach are that 1) the use of a ''frozen'' model eliminates the discontinuities associated with model changes that have occurred over the periods spanned by operational analyses, and 2) a reanalysis incorporates all available data from diverse sources, including data received too late for inclusion in operational analyses. It is likely that many of the NP observations, especially from the era preceding satellite telecommunications, fall into this category of ''late reports.''

This study uses the reanalysis products from two major centers: NCEP (National Centers for Environmental Prediction), see Kalnay et al. (1996), and ECMWF (European Centre for Medium-Range Weather Forecasts), see Gibson et al. (1997). The resolution of the models used in the reanalyses is T62 (approximately 210 km) for NCEP and T106 (approximately 120 km) for ECMWF; most of the archived output is four times daily at a resolution of 2.5° lat $\times$ 2.5° long. Our computations summarized in the following section are based on 11 yr (1985–95) of the NCEP reanalysis and 14 yr (1980–93) of the ECMWF reanalysis. For the comparison with the Russian ice station measurements, we composited the

reanalysis output over a subset of 11 of the 2.5° × 2.5° grid points in the central Arctic (Fig. 1).

All values of the reanalysis output used in this study are daily means. In the cases of surface air temperature, wind speed, and sea level pressure, the means are computed from the instantaneous values at 0000, 0600, 1200, and 1800 UTC. In the cases of the radiative fluxes and cloudiness, the means are computed from the corresponding four 6-h means archived in the reanalysis output files. Each 6-h value of model-derived variable (radiative flux, cloudiness, precipitation . . .) in the reanalysis output is the average over a 6-h forecast: the 12–18-h forecast in the ECMWF reanalysis and the 0–6-h forecast in the NCEP reanalysis. While the choice of the 12–18-h forecast of the ECMWF model was made in order to reduce the effects of model ''spinup,'' NCEP's use of a three-dimensional variational analysis scheme (rather than an optimum interpolation scheme) has been found to produce a major reduction in the spinup (Kalnay et al. 1996, 445). Hence the short-range forecasts of the NCEP reanalysis model are used by most investigators. Jacob (1994) has shown that there is also very little spin up in the cloud cover and radiative fluxes of the ECMWF system.

The AARI observational values are handled in a manner consistent with our use of the reanalysis output. The surface air temperature, wind speed, sea level presure, and cloud fraction are averages of four instantaneous (6-h) measurements at the ice station, while the radiation fluxes are averages of continous measurements made over the 24-h period.

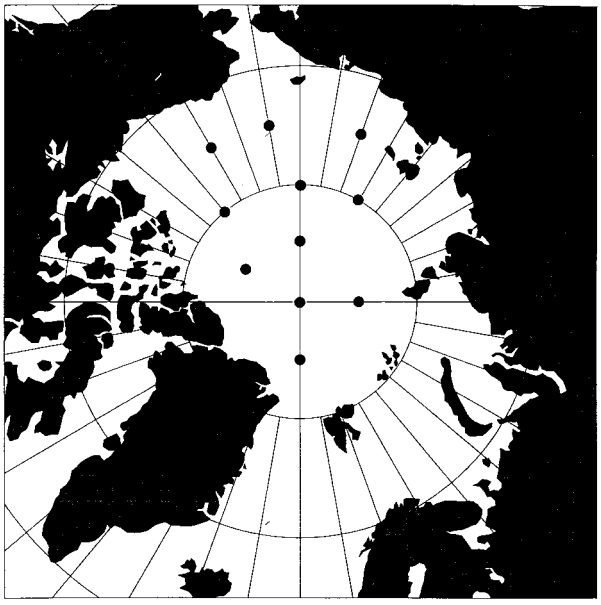

FIG. 1. Grid points over which NCEP and ECMWF reanalysis output was averaged.

3. Results

a. Synthesis of observations

Because associations with cloudiness are the focus of this study, we first show an inventory of the AARI (NP) reports of cloud fraction. Figure 2 indicates that several thousand such reports are available for most years from the mid-1950s to 1990. The yearly totals are consistent with a reporting frequency of 6 h and the presence of two–three stations.

In order to stratify the AARI observations on the basis of cloudiness, the individual reports were categorized as ''cloudy,'' ''partly cloudy,'' and ''clear'' when the reported cloud fractions (CF) were in the respective ranges $CF \geq 0.8$, $0.2 < CF < 0.8$, and $CF \leq 0.2$. The individual days were classified similarly according to the daily mean values of CF. Figure 3 shows the seasonal climatology of Arctic cloudiness in terms of the relative frequencies of cloudy and clear reports. From November through April, cloudy and clear conditions were each reported approximately 40% of the time; the remaining 20% of the reports were in the partly cloudy category. The mean wintertime values of 0.50–0.55 are comparable to the International Satellite Cloud Climatology (ISCCP) derived values reported by Rossow et al. (1993), while the mean summertime values of 0.75–0.80 are much higher than the corresponding summer values from ISCCP (Curry et al. 1996, their Fig. 1). However, revised ISCCP values presented by Rossow (1995) are in the 0.65–0.70 range for both January and July. By including the so-called marginal cloud amounts, Schweiger and Key (1994) obtain ISCCP values of 0.60–0.70 for winter and 0.50–0.60 for summer in the region poleward of 62.5°N. Revised estimates based on surface reports from the same region are approximately 0.60 for winter and 0.80 for summer (Warren et al. 1988), although Hahn et al.'s (1995) more recent surface-based estimates for January are closer to 0.65. Curry and Ebert's (1992) wintertime estimates of approximately 0.8 are even higher because they include a contribution from lower-tropospheric ice crystal precipitation. One may assume that the AARI cloud fractions do not include ice crystal precipitation. However, we note that the frequency of wintertime clear-sky reports in the AARI data decreases from about 50% in the 1950s to about 30% in the 1980s, suggesting the possibility that ice crystal precipitation may be included in the cloud reports with increasing frequency in the later portion of the dataset.

The rapid increase of cloudy reports in May mirrors the decrease of clear reports in Fig. 3. Cloudy conditions were reported more than 80% of the time in June–September, and clear conditions were reported in less than 10% of the cases. While the abrupt springtime increase and autumn decrease in low stratus are well known from earlier climatologies (e.g., Huschke 1969; Warren et al. 1988; Curry et al. 1996), Fig. 3 illustrates the bimodality of cloud cover in the Arctic; cloud fractions between 0.2 and 0.8 occur relatively infrequently (less than 20%–

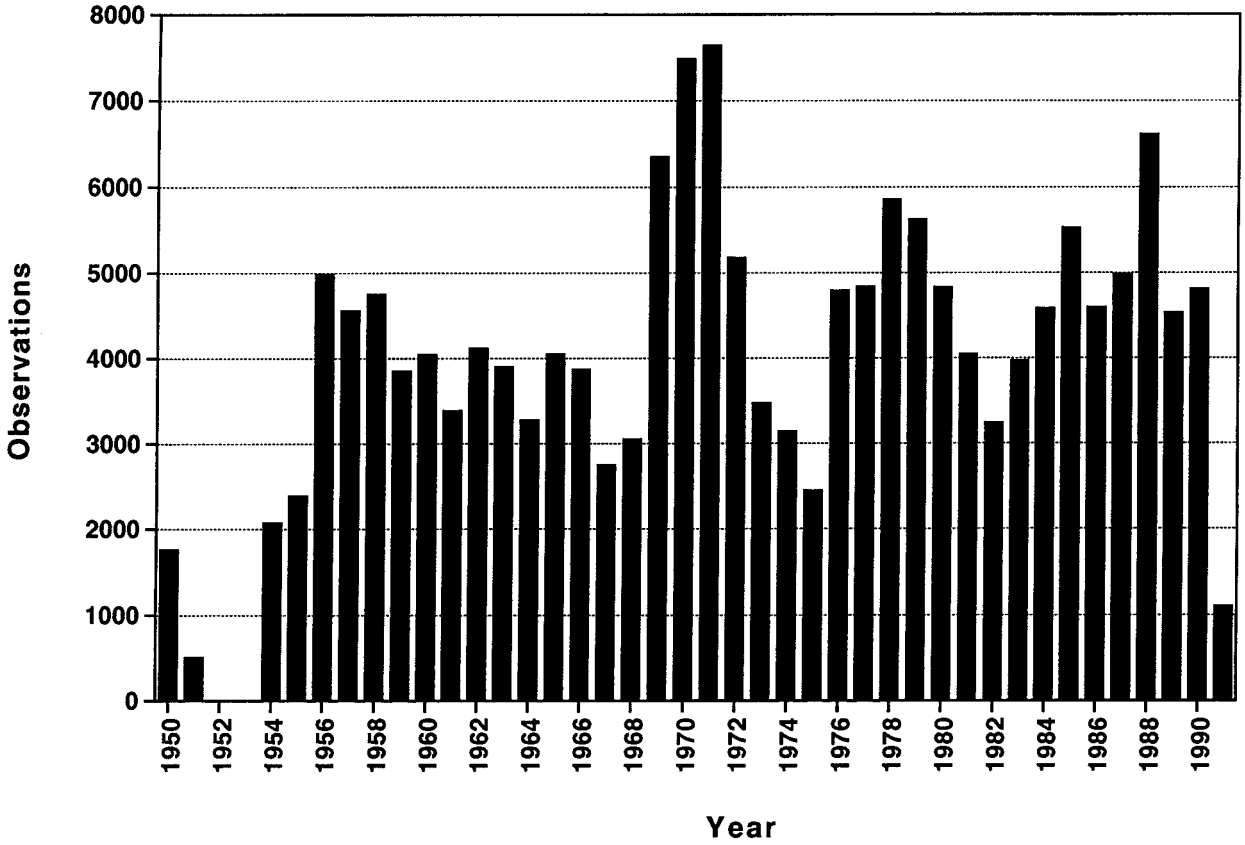

FIG. 2. Yearly numbers of archived cloud observations in the Russian (AARI) ice station database.

30% of the time), at least according to the reports from the drifting ice stations. While partly cloudy conditions can be difficult to detect during the polar night (cf. Hahn et al. 1995), we note here that partly cloudy reports are no more frequent during the cloudy summer months than during the winter.

As found in earlier analyses of the drifting ice station reports (R. Colony 1992, personal communication), Arctic cloudiness varies in association with other near-surface weather variables. Figure 4 shows that sea level pressures tend to be lower under cloudy conditions than under clear conditions. The pressure differences are typically 7–10 mb and are even larger during the summer,

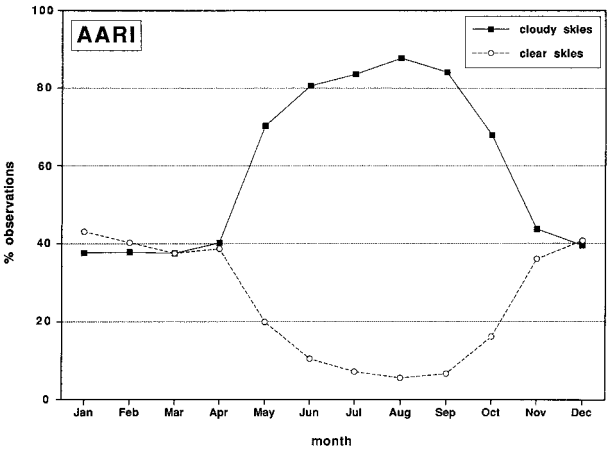

FIG. 3. Monthly percentages of ice station observations in which reported sky conditions were cloudy (CF $\geq$ 0.8) and clear (CF $\leq$ 0.2).

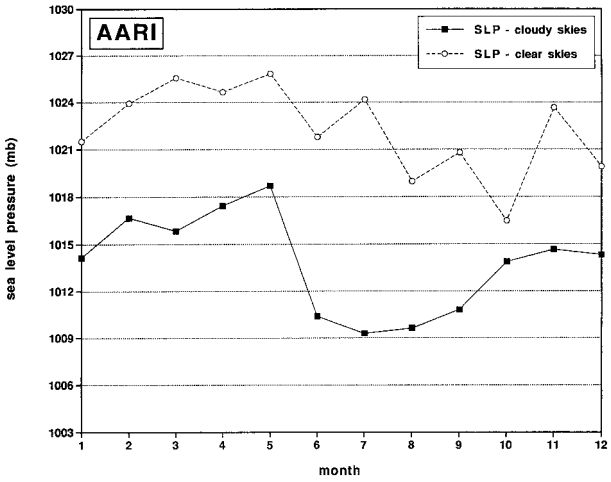

FIG. 4. Annual cycle of mean sea level pressures from all AARI ice station reports for days categorized as cloudy (solid squares) and clear (open circles).

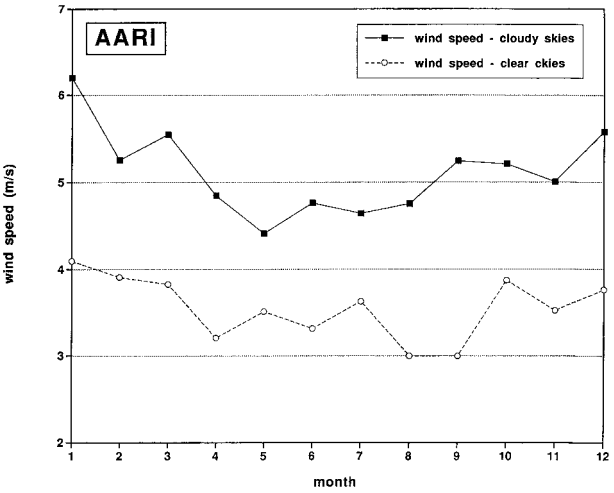

FIG. 5. Annual cycle of mean wind speed from all AARI ice station reports for days categorized as cloudy (solid squares) and clear (open circles).

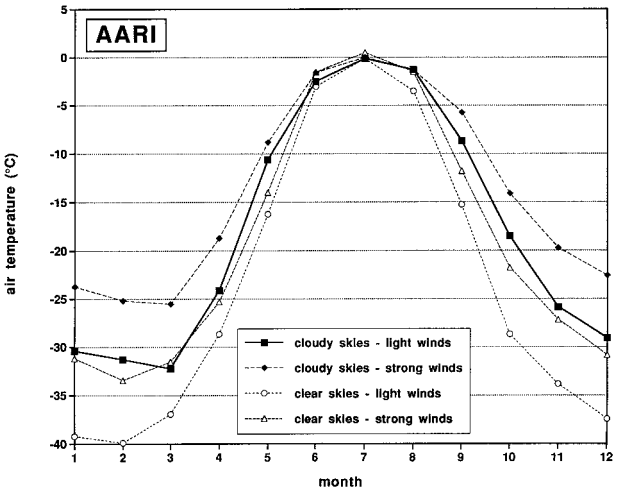

FIG. 6. Annual cycle of mean surface air temperature from all AARI ice station reports for days having various combinations of sky cover and wind speed. Sky cover and wind speed categories are defined in text.

approaching 15 mb in July. These differences point to a contribution by synoptic-scale systems to the day-to-day variations in Arctic cloudiness, even (and especially) during the summer melt period when much of the cloudiness is boundary layer stratus and fog.

In order to illustrate the association between Arctic cloudiness and surface wind speed, Fig. 5 shows the wind speeds averaged over all cloudy days and all clear days of each calendar month. The wind speeds under cloudy conditions are typically about 50% greater than under clear conditions. The differences are consistent with the notions of greater moisture advection (assuming that wind speed is more important than wind direction in determining the influx of moisture to the central Arctic) and greater turbulent mixing of momentum as well as moisture when the sky is cloudy. Conversely, relatively light winds occur under clear skies when near-surface temperature inversions are most likely to inhibit vertical mixing of momentum.

The association between cloudiness and wind speed was extended to include surface air temperature by grouping the daily means into three categories of wind speed. This grouping was done by evaluating the 33 and 67th percentiles of daily mean wind speed for each calendar month, thus permitting the categorization into terciles of ''light,'' ''moderate,'' and ''strong'' winds appropriate to the season. By pairing the wind categories with the cloud categories defined earlier, we can place each daily value into a 3×3 matrix of wind and cloudiness: light winds and cloudy, strong winds and partly cloudy, moderate winds and clear, etc. Figure 6 shows the seasonal cycle of surface air temperature for the four ''corner'' elements of the 3×3 matrix: strong winds and clear, strong winds and cloudy, light winds and clear, light winds and cloudy. It is apparent from Fig. 6 that the air temperature varies systematically with both cloudiness and wind speed, especially in the nonsummer months. The highest temperatures occur with cloudy skies and strong winds, while the lowest temperatures occur with clear skies and light winds; the mean temperatures for these two categories differ by approximately 15°C from October through February. Overland and Guest (1991) found that snow surface temperatures north of Svalbard during 1988–89 underwent similar day-to-day changes during transitions between clear and overcast skies. Figure 6 shows that the effect of a change from one extreme to the other extreme of wind has about the same impact (in °C) as a change from one extreme of cloudiness to the other, at least during the winter half of the year. For a brief period during summer, when temperatures are relatively constant over melting snow and ice, the wind speed becomes the more effective discriminator. The temperatures during June, for example, are higher by 1°–2°C with strong winds regardless of the cloud cover. One implication of Fig. 6 is that models will need to capture the physics underlying the associations between temperature and wind, as well as cloudiness, if they are to provide realistic simulations of the temporal variations of surface air temperatures in the Arctic.

The underlying physics in the associations described above almost certainly involve the radiative fluxes and their interactions with clouds. Clouds can be expected to enhance the downward flux of longwave radiation at the surface and to reduce the downward flux of solar radiation at the surface. Studies based on models of Arctic radiative transfer and surface interactions indicate that the longwave effect of Arctic clouds predominates over the shortwave effects throughout the year except for a few weeks during the summer melt (Curry and Ebert 1992). This result is generally consistent with the ISCCP analyses (Schweiger and Key 1994, their Fig. 4; Curry et al. 1996, their Fig. 10), although the ISCCP

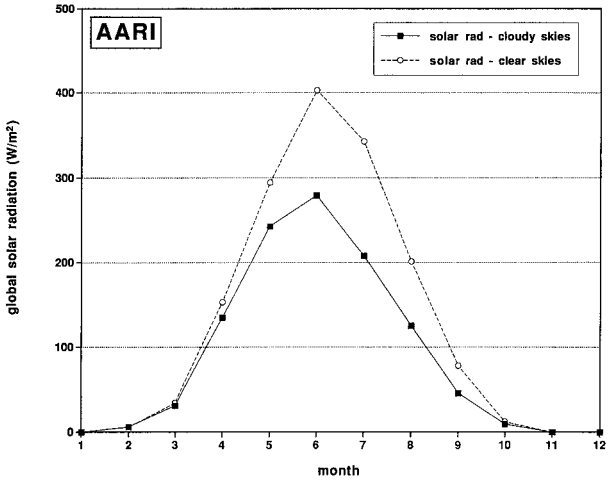

FIG. 7. Annual cycle of mean global solar radiation (incoming direct plus diffuse) from all AARI ice station reports for days categorized as cloudy (solid squares) and clear (open circles).

data suggest that the shortwave cooling effect may exceed the longwave warming for a somewhat longer summer period than a few weeks. Isaac and Stuart's (1996) analysis of northern land station data for January and July also showed that clouds are associated with higher winter temperatures and lower summer temperatures, although radiative flux data were not included in Isaac and Stuart's study.

Figure 7 shows the seasonal cycle of downward solar radiation at the Arctic surface based on composites of all cloudy and all clear daily means from the drifting ice stations. The downward solar flux is greater under clear skies by amounts ranging from several W m^{-2} when the solar elevation angle is small (March, October) to more than 100 W m^{-2} in June and July. The monthly values peak during June at approximately 400 W m^{-2} under clear skies and 275 W m^{-2} under cloudy skies. It should be noted that the values for cloudy skies include the effects of multiple reflections between the clouds and the surface; Shine (1984) shows that these effects can be substantial when the surface is highly reflective and a low overcast is present. During the summer months the actual (''all days'') monthly means are closer to the values for cloudy skies in Fig. 7 because cloudiness is so widespread during the summer. The all-case means peak at approximately 310 W m^{-2}, which is very close to the summertime peak value of approximately 320 W m^{-2} in the model results of Curry and Ebert (1992), the comparable ISCCP-derived values for July 1985 found by Rossow and Zhang [(1995); see Fig. 2 of Curry et al. (1996)], and the somewhat smaller ISCCP-derived peak value of 285 W m^{-2} found by Schweiger and Key (1994). In this regard, we note that the downward solar flux reaching the surface is one of the variables for which means over heterogeneous surface types should not differ substantially from the point measurements made over thick ice. By contrast, the reflected solar radiation (Fig. 8a) will depend strongly on the surface type. The values in Fig. 8a can be assumed to be representative of only the thick ice floes on which the Russian instrumentation was sited. The reflected solar fluxes from such surfaces exceed 200 W m^{-2} in May–June and are larger under clear-sky conditions because the downward fluxes at the surface are larger when clouds are absent. The surface albedo, computed as the ratio of the reflected to the incident solar fluxes, is shown in Fig. 8b for the months when the incident solar flux exceeds 10 W m^{-2}. The clear-sky albedo ranges from 0.81 in the spring to a minimum of 0.58 in July, when the surface typically loses all or most of its snow. The cloudy-sky albedo exceeds the clear-sky surface albedo because clouds selectively absorb the longer wavelengths, for which the surface reflectivity is smaller. The difference between the cloudy- and clear-sky albedo ranges from 0.02–0.03 in March and April to 0.06–0.09 in June and July. As in the case of the reflected solar fluxes, the all-case mean values of surface albedo are closer to the cloudy-sky values because of the prevalence of cloud cover in the months when the solar ra-

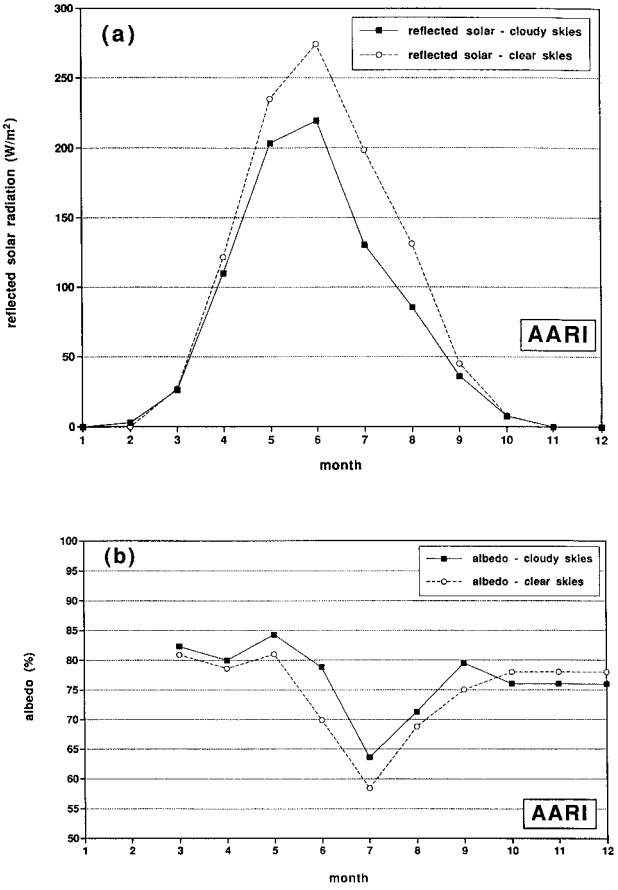

FIG. 8. Annual cycles of (a) surface reflected solar radiation and (b) surface albedo averaged over all AARI ice station reports for days categorized as cloudy (solid squares) and clear (open circles). Albedo values are plotted only for months in which incident solar flux exceeds 10 W m^{-2}.

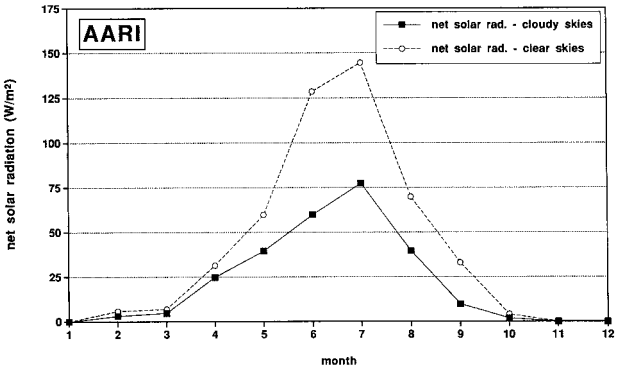

FIG. 9. Annual cycle of surface net solar radiation averaged over all AARI ice station reports for days categorized as cloudy (solid squares) and clear (open circles).

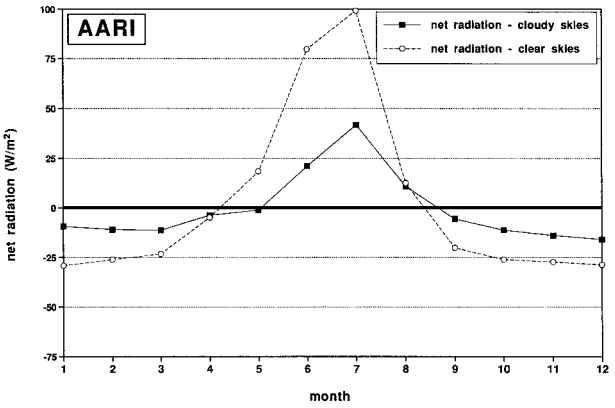

FIG. 10. As in Fig. 9, but for surface net total radiation (net solar + net longwave).

diation is strongest. We reiterate the earlier caveat that the results pertaining to surface albedo are valid only for thick floes and for locations considered unlikely to ''flood,'' that is, the impact of summer melt ponds has been minimized by the site selection.

Figure 9 shows the annual cycles of net solar radiation (downward minus upward) for the clear-sky and cloudy-sky cases in the AARI data. The values in Fig. 9 represent the solar radiation absorbed by the surface. For comparison with the results from the reanalyses, we note that the net solar flux reaches its peak in July at 142 W m^{-2} under clear skies and 77 W m^{-2} under cloudy skies. The July peak in the net solar flux occurs one month later than the June peak in the downward solar flux because of the substantial decrease of surface albedo from June to July (Fig. 8b).

The ice station archives also include values of the net radiation measured at the surface. The net radiation includes the solar and longwave fluxes. The monthly means of the net surface radiation for the cloudy- and clear-sky cases are shown in Fig. 10. The net surface radiation is negative (upward) from September through April, both with and without clouds. Clouds reduce the positive (downward) net flux in May, June, and July, implying that clouds have a net cooling effect in those months. Clouds have a net warming effect in September–March, while they have little impact on the net radiation in April and August. The cloudiness-weighted mean of the two curves in Fig. 10 shows general agreement with the ISCCP-derived fluxes of Rossow and Zhang [(1995), plotted in Curry et al.'s (1996) Fig. 4)] and Schweiger and Key (1994, their Table 2) although the summer maximum of the cloudiness-weighted values in Fig. 10 is approximately 80 W m^{-2}, which is slightly smaller than the maximum of approximately 100 W m^{-2} in the ISCCP-derived values. Key et al. (1997) note that instantaneous satellite retrievals have uncertainties as large as 41 W m^{-2}; uncertainties in monthly mean values will be smaller.

The net cloud-radiative forcing (CRF) has conventionally been defined as the difference between the net surface radiative flux under the cloud fraction CF and the net surface radiative flux under clear skies (Curry and Ebert 1992). Climatological values of the conventional cloud-radiative forcing are thus based on the climatological cloud fractions, which are in the range $0 \leq CF \leq 1$. The differences between the two curves in Fig. 10 represent upper bounds on cloud-radiative forcing because the cloudy days are essentially completely cloudy ($CF \geq 0.8$). If the solid curve in Fig. 10 were based on all days, it would depict the fluxes used in conventional evaluations of cloud-radiative forcing. We will use the term maximum cloud-radiative forcing (MCRF) to denote the difference between the two curves in Fig. 10. The sign of the conventional cloud-radiative forcing should be the same as the sign of the MCRF, implying that the cloud-radiative forcing is negative for the months of May, June, and July. The 3–4-month period of negative MCRF (and hence CRF) is longer than Curry and Ebert's (1992) ''two weeks,'' but very similar in duration to the period of negative CRF obtained from the ISCCP data by Schweiger and Key (1994, their Fig. 4) and by Rossow and Zhang [(1995), plotted in Fig. 10 of Curry et al. (1996)]. When the cloudy curve in Fig. 10 is adjusted for the climatological cloud fractions by including all days, the maximum negative cloud-radiative forcing (in July) is close to Schweiger and Key's ISCCP-derived value of 40–50 W m^{-2} and the Curry and Ebert value of 50 W m^{-2} (Curry et al. 1996, their Fig. 10).

In order to bring the AARI radiative measurements into a framework that permits more direct comparisons with the conventional ''cloud-radiative forcing,'' Fig. 11 shows the differences between the cloudy-sky net surface flux and the clear-sky net surface flux as a function of cloud fraction and month. The color bar, which is not symmetric about zero, is such that the yellow, orange, and red shades denote warming (greater incoming net radiation) under the cloud fraction CF relative to $CF = 0$, while the blue shades denote cooling (smaller net incoming or greater net outgoing radiation) under cloud fraction CF relative to $CF = 0$. It is apparent from

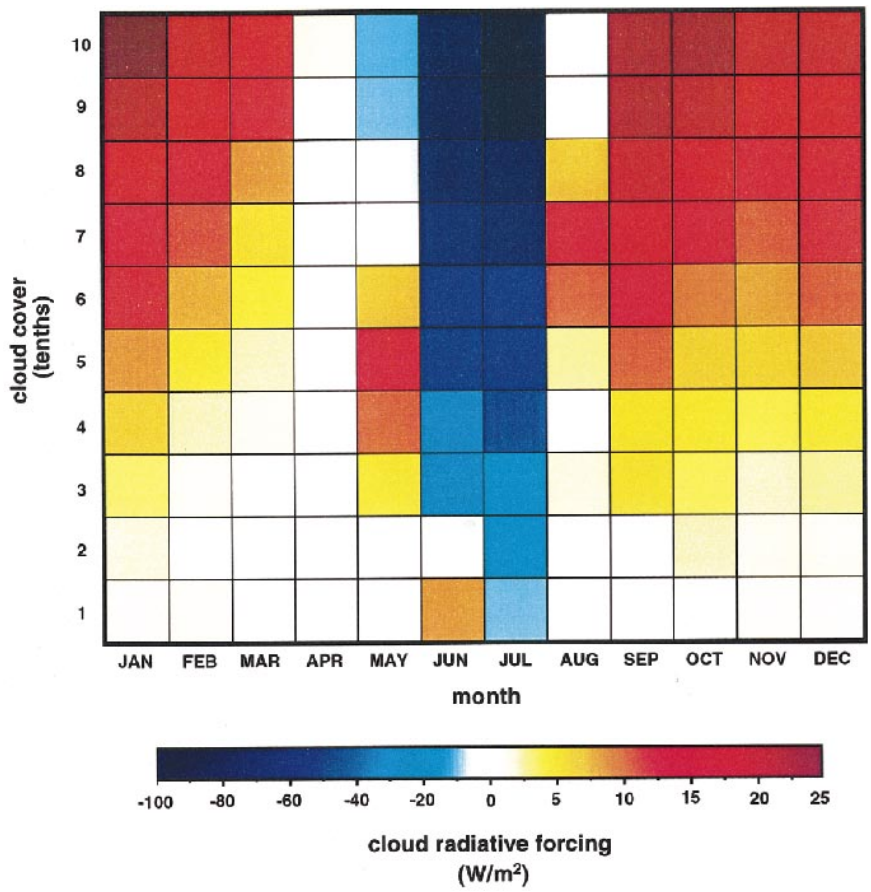

FIG. 11. Annual cycles of differences between net surface radiation (cloud fraction > O) and clear-sky net surface radiation. Differences are shown as functions of calendar month (abscissa) and cloud cover (ordinate). Blues denote negative differences, yellows and reds positive differences.

Fig. 11 that clouds cool the surface in June and July for essentially all values of cloud fraction CF. The effect of clouds is close to zero in April and May, in contrast to the situation over northern land areas, for example, Barrow, where Zhang et al. (1996) find positive cloud-radiative forcing during the May snowmelt. While clouds also have little net radiative impact on the surface in August, their radiative effect is positive (warming of the surface) for essentially all cloud fractions from September through March. The largest positive values, 20–30 W m^{-2}, occur during the autumn and winter when CF exceeds 0.8.

Figure 11's large negative values in the summer months must be accompanied by two important caveats. First, as noted in section 1, the observations summarized here do not take into account the surface heterogeneities that may impact the values of the cloud-radiative forcing. One of the attractive possibilities offered by SHEBA, ARM, and FIRE is the improvement of Fig. 11 by the inclusion of the effects or surface heterogeneities. The second caveat is that the AARI ice station archives include relatively few daily mean values of clear-sky net radiation during the summer months, when it is uncommon for skies to remain clear throughout the day. The number of days for which such values are provided is only 5–10 for June and July. Moreover, the net radiative fluxes for July and August of 1986 could not be used because they were found to be identical to the direct solar radiation and therefore suspect. Thus the statistical validity of the clear-sky values on which the middle columns of Fig. 11 are based is not as high as for the wintertime columns, which are based on samples containing far more clear-sky days. The noise in individual columns (e.g., April, May, August) of Fig. 11 is an indication of the small sample sizes.

The AARI ice station data archived at NSIDC do not include the net longwave fluxes at the surface. However, the net longwave fluxes may be obtained as the differences between the net total fluxes and the net solar fluxes. Maykut and Church (1973) used this procedure to obtain longwave fluxes for Barrow, Alaska. We have evaluated these differences from the daily ice station data. As shown in Fig. 12, the net longwave fluxes evaluated in this manner are negative in all calendar

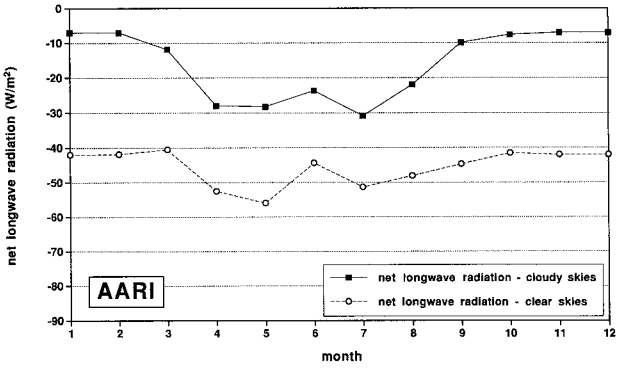

FIG. 12. Annual cycle of surface net longwave radiation derived from net total radiation and net solar radiation averaged over all AARI reports for days categorized as cloudy (solid squares) and clear (open circles).

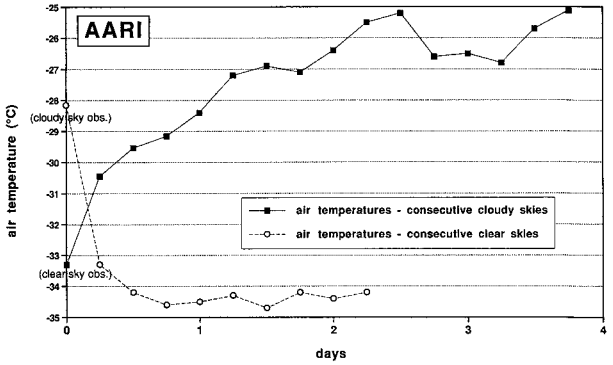

FIG. 13. Mean surface air temperature at ice stations as a function of time after a transition from cloudy-to-clear (open circles) and clear-to-cloudy (solid squares) during the winter portion of the year, November–March.

months under both cloudy and clear skies, indicating a net loss of longwave radiation from the surface. However, the loss is smaller under cloudy skies in all months, especially during the winter. The net longwave loss under both cloudy skies and clear skies increases from winter to summer. The cloudiness-weighted net surface longwave fluxes are comparable to the ISCCP-derived fluxes of Schweiger and Key (1994, their Fig. 3), although the ISCCP net longwave fluxes are generally larger by 10–40 W m^{-2} than the cloudiness-weighted means of the fluxes in Fig. 12. The values in Fig. 12 imply a longwave maximum cloud radiative forcing of 20 W m^{-2} (summer) to 30 W m^{-2} (winter), which is somewhat smaller than Schweiger and Key's (1994, their Fig. 4) ISCCP-derived longwave forcing and Curry and Ebert's (1992, their Fig. 9) model-derived longwave forcing. However, we note again that the data used here are for points located intentionally away from leads, thin ice, and melt ponds, which should have radiative regimes different from thick ice.

Figures 11 and 12 show that clouds reduce the net loss of radiation (primarily longwave) at the Arctic surface during the winter months. This dependence of radiative fluxes on cloudiness is consistent with the higher temperatures under cloudy skies (vs clear skies) during winter. Since the positive wintertime cloud-radiative forcing must contribute to the warming under clouds, the timescale of the warming response is relevant to successful simulation of the Arctic energy budget. Figure 13 shows that a transition from clear to cloudy skies during winter (November–March) is followed by a gradual warming of 5°–6°C over approximately 48 h. Similarly, a transition from cloudy to clear skies is followed by cooling over approximately 12 h. The transition to the full cloudy–clear difference of temperature thus appears to have a timescale of a half day to several days, which may be regarded as an equilibration time of the Arctic surface energy budget over thick ice during winter. This timescale is consistent with Overland and Guest's (1991, their Fig. 17) model simulations of snow temperatures in the Coordinated Eastern Arctic Experiment region during transitions between cloudy and clear conditions.

b. Comparison with reanalyses

The distributions of Arctic cloudiness are strikingly different in the NCEP and ECMWF reanalyses. As shown in Fig. 14a, the NCEP cloud fractions are nearly identical in summer and winter; the NCEP fractions are distributed over a broad range with the highest frequencies between 0.3 and 0.7. By contrast, the ECMWF distribution (Fig. 14b) shows a strong bimodality (either no clouds or complete overcast) during winter and a preponderance of overcast or near-overcast during summer. The seasonality of the ECMWF monthly mean cloud fractions shows a much closer correspondence with the observationally derived fractions (Fig. 3). It should be noted that cloud coverage is not directly assimilated from observations during a reanalysis; rather, it is determined by the models' respective cloud parameterization schemes [cf. Kanamitsu et al. (1991) for NCEP; Tiedtke (1993) and Jacob (1994) for ECMWF].

The daily means of the reanalysis-derived surface air temperatures from both centers were composited according to cloud coverage by the same criteria used with the AARI ice station reports. Figures 15a,b show that both reanalyses capture the seasonality and actual values of air temperature, although the ECMWF temperatures appear to be too high by several degrees Celsius during winter, especially with clear skies, and too low by several degrees Celsius during summer relative to the AARI observations (Fig. 15c). Moreover, the association between temperature and cloudiness is undercaptured by the ECMWF reanalysis, which shows cloudy–clear differences of only 2°–4°C during the nonsummer months. The observed differences in Fig. 15c are 8°–10°C during October–February and 5°–6°C during March–May and September. The NCEP temperatures (Fig. 15a), on the other hand, appear to be oversensitive to cloudiness dur-

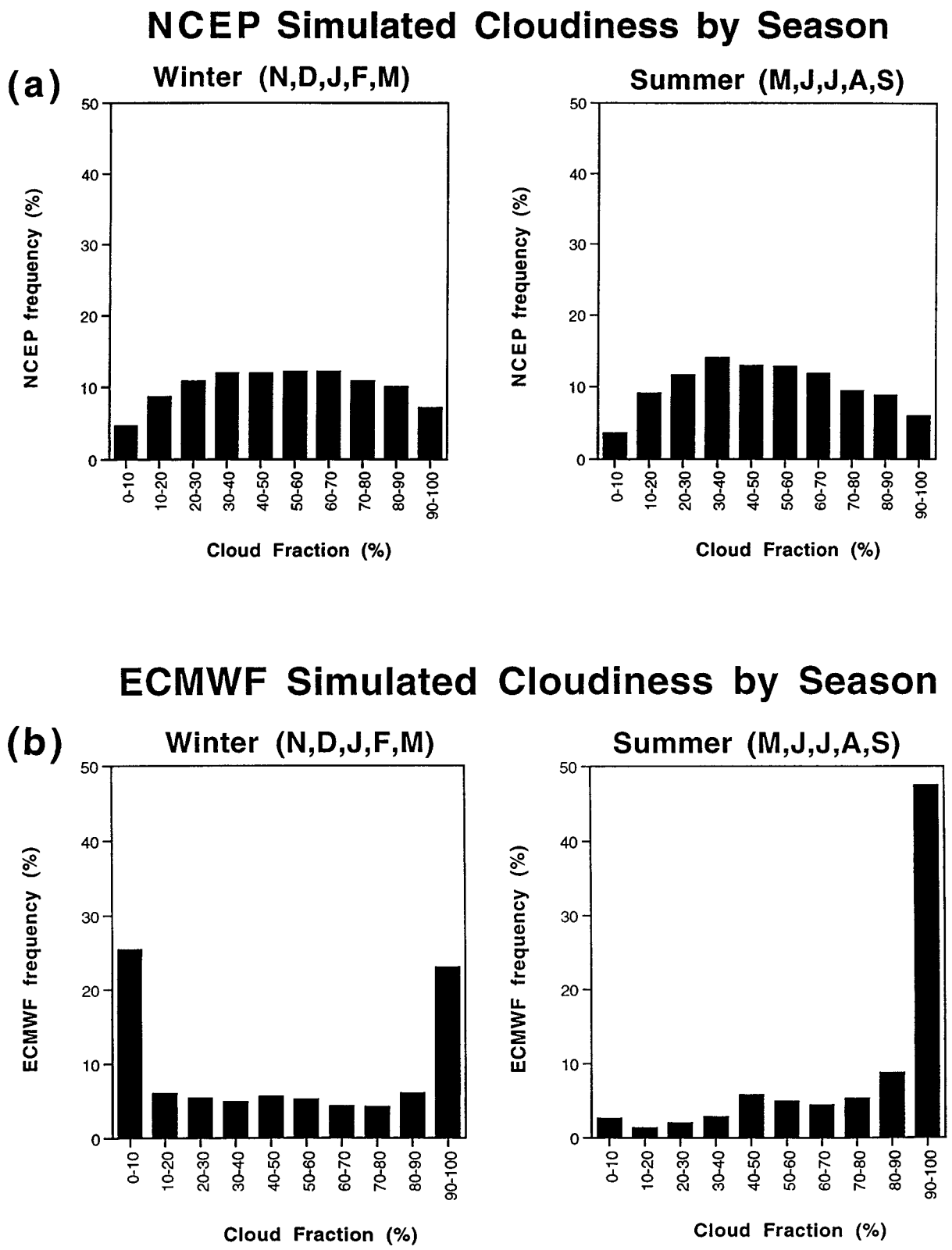

FIG. 14. Histograms of cloud coverage (%) during winter (November–March) and summer (May–September) at the grid points of Fig. 1 in the reanalyses of (a) NCEP and (b) ECMWF.

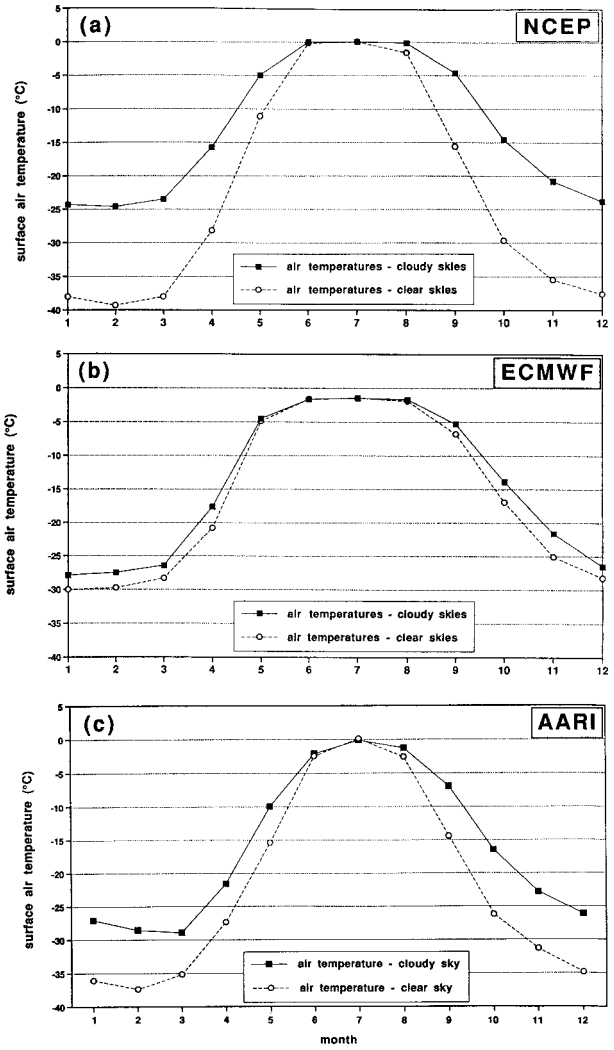

FIG. 15. Annual cycles of mean surface air temperature averaged over all days categorized as cloudy (solid squares) and clear (open circles) in (a) the NCEP reanalysis, (b) the ECMWF reanalysis, and (c) AARI ice station observations.

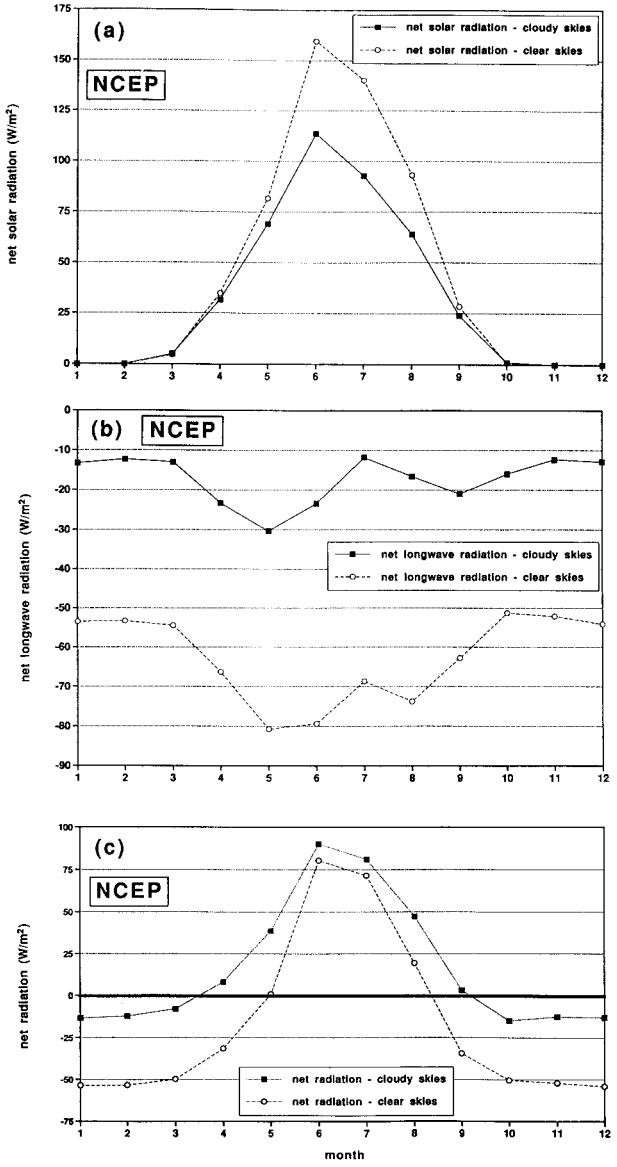

FIG. 16. Annual cycles of (a) net surface solar radiation, (b) net surface longwave radiation, and (c) net surface total radiation from the NCEP reanalysis averaged over all days categorized as cloudy (solid squares) and clear (open circles).

ing the September–April period, although the oversensitivity is generally less than about 5°C.

Figure 16 shows the annual cycles of the surface radiative fluxes stratified by cloudiness in the NCEP reanalysis. The net shortwave fluxes in Fig. 16a are generally slightly larger than the corresponding observational fluxes obtained by subtracting the AARI reflected solar fluxes (Fig. 8a) from the incident solar fluxes (Fig. 7). Table 1 summarizes the NCEP and AARI solar fluxes; the differences in the clear-sky fluxes of May, June, and August are indicative of a lower surface albedo in the NCEP reanalysis.

The discrepancies in the cloudiness-weighted mean fluxes are attributable to differences in cloudiness as well as surface albedo. When averaged over all days, the net surface solar flux in the NCEP reanalysis peaks at 139 W m^{-2} in June, which compares to Schweiger

TABLE 1. Monthly means of net solar fluxes (W m^{-2}) for clear days and cloudy days from NCEP reanalysis and AARI data.

	Clear sky		Cloudy sky	
	NCEP	AARI	NCEP	AARI
April	37	35	33	25
May	80	60	68	40
June	160	135	112	60
July	140	140	90	80
August	92	65	62	45

and Key's (1994, their Fig. 2) ISCCP-derived peak value of 160 W m^{-2} in July and Curry and Ebert's (1992, their Fig. 9) model-derived peak of 120 W m^{-2} in July. As shown in Fig. 9, the AARI net solar flux also peaks in July. While the cloudiness-weighted mean of the AARI net solar fluxes for July is approximately 100 W m^{-2}, this value does not include the effects of leads and open water in enhancing the surface absorption of solar radiation. The earlier peak of the NCEP shortwave flux is consistent with a lower surface albedo prior to the disappearance of the snow in July.

The net longwave fluxes in the NCEP reanalysis (Fig. 16b) agree well with the AARI longwave fluxes in Fig. 12, although the increased magnitude of the negative clear-sky fluxes in the reanalysis occurs earlier (April) than in the AARI data. The all-sky values of -30 to -50 W m^{-2} are very consistent with those of Schweiger and Key (1994, Fig. 3) and Curry and Ebert (1992, Fig. 9) When the net total (solar plus longwave) fluxes in Fig. 16c are compared with those from the other sources, the differences are largest in summer and are attributable primarily to the solar fluxes (Fig. 16c vs Fig. 9).

In all months in which there is solar radiation, clouds reduce the net surface solar radiation and increase the net surface longwave radiation in both the reanalyses and the AARI observational data. Thus the solar component of the maximum cloud radiative forcing (and, by implication, the CRF) is negative in all months, while the longwave component is positive in all months. The numerical values of the net MCRF from the reanalyses and the observational data are compared at the conclusion of this section.

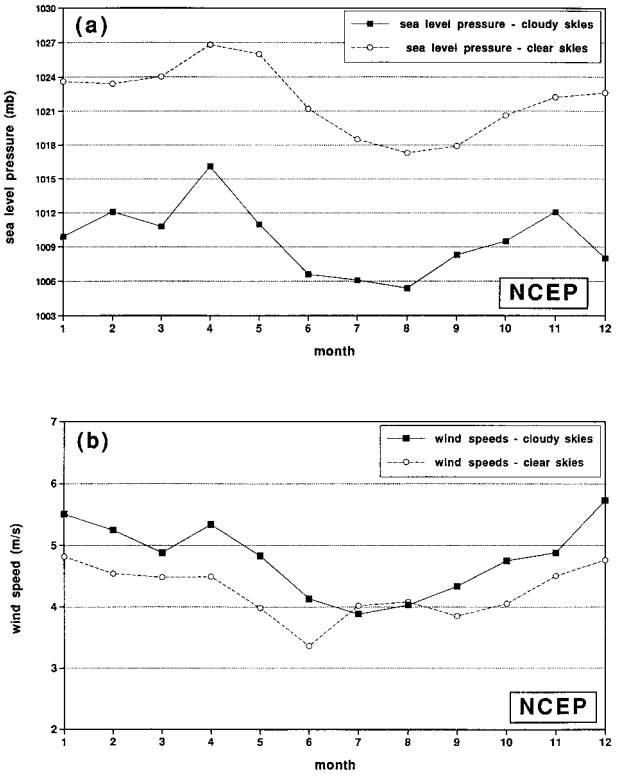

FIG. 17. Annual cycles of (a) sea level pressure and (b) surface wind speed from the NCEP reanalysis averaged over all days categorized as cloudy (solid squares) and clear (open circles).

Figure 17a shows that the NCEP reanalysis captures the observationally derived association between cloudiness and sea level pressure, although the reanalysis's pressure differences (clear–cloudy) are somewhat larger than observed during winter. One may thus infer that the controls on cloudiness by synoptic weather systems are captured by the reanalysis. It is also apparent that the seasonal cycle of sea level pressure is captured well by the reanalysis, although this outcome is not surprising because pressures are assimilated directly from the observational measurements. On the other hand, the association between cloudiness and wind speed is weaker in the reanalysis (Fig. 17b) than in the observational data (Fig. 5). Although the signs of the wind speed differences (cloudy–clear) are generally consistent with observations, the magnitudes of the differences are less than half the observed in most months. There are no surface wind reports from the central Arctic to be assimilated directly into the reanalysis.

The seasonal cycles of the surface radiative fluxes in the ECMWF reanalysis are shown in Fig. 18, which is the counterpart of Fig. 16 for NCEP. The longwave fluxes again show the anticipated dependence on cloudiness, as the net longwave loss (upward flux) is greater by 5–10 W m^{-2} under clear skies (Fig. 18b). However, the implied longwave forcing by cloudiness is smaller than in the observational data for autumn and winter (Fig. 12), much smaller than the corresponding NCEP values (Fig. 16b), much smaller than in the ISCCP results of Schweiger and Key (1994, their Fig. 4), and much smaller than Curry and Ebert's (1992, their Fig. 9) model-derived surface longwave forcing by clouds. A more puzzling feature of the ECMWF output is the absence of an impact of clouds on the net solar radiation at the surface. Figure 18a shows that, while the surface solar fluxes follow a realistic seasonal cycle, they do not vary systematically between the two extremes of cloud cover. The numerical values are closer to the clear-sky than to the cloudy-sky values from the other sources. Since the solar fluxes dominate the annual cycle, the plot of the net total surface fluxes in Fig. 18c resembles Fig. 18a. The ECMWF solar fluxes at the Arctic surface evidently require closer scrutiny before they are used in diagnostic applications. The ECMWF net solar fluxes peak at approximately 95 W m^{-2} in June. The magnitude of this peak is very close to, but a month earlier than, the maximum in the AARI fluxes for thick ice (Fig. 9).

Finally, Fig. 19 summarizes the maximum cloud radiative forcing (solar plus longwave) from the three sources. The observationally derived values from the AARI data are positive in all months from September through April and negative from May through July. The

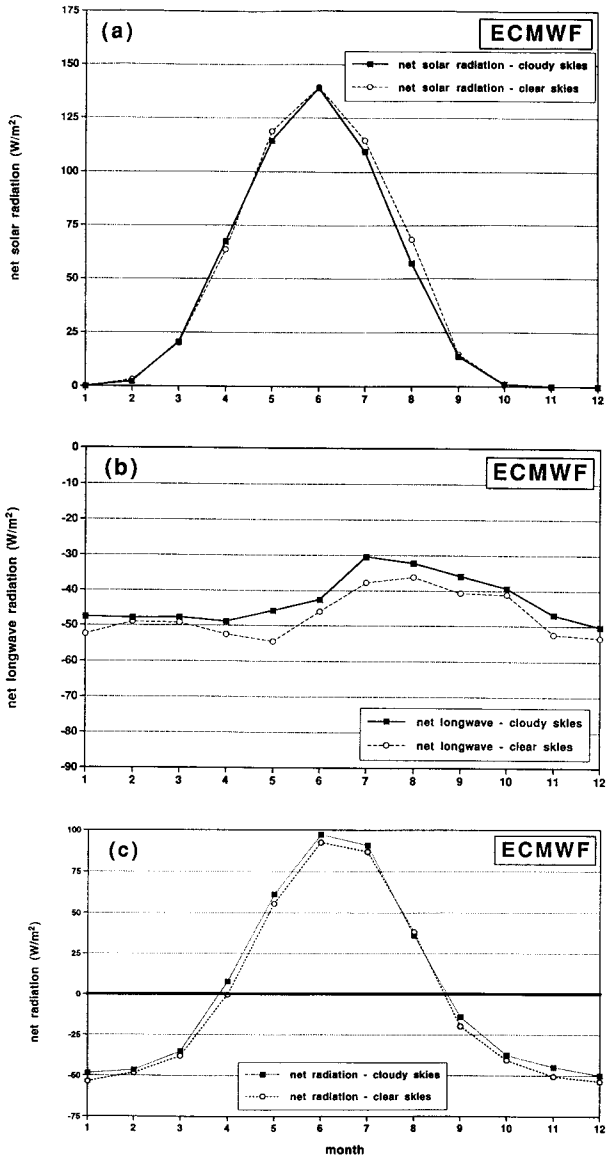

FIG. 18. As in Fig. 16, but for the ECMWF reanalysis.

values range from 20–30 W m^{-2} in autumn and winter (September–February) to the June minimum of -59 W m^{-2}. Neither reanalysis captures the essential characteristics of this seasonal cycle: the NCEP values remain positive in all months, although their autumn and winter values are close to those obtained from the AARI data; the ECMWF values are close to zero in all months and show no seasonality, primarily because clouds do not impact the surface solar radiation. On the other hand, the AARI values of MCRF in Fig. 19 agree well, both qualitatively and quantitatively, with seasonal cycles of Arctic CRF obtained by Schweiger and Key (1994, their Fig. 4) and Rossow and Zhang (1995). While there are differences in the length of the summertime period of negative forcing and differences of 10–20 W m^{-2} in the wintertime values relative to Curry and Ebert (cf. Curry et al. 1996, their Fig. 10), the agreement is surprisingly good considering that 1) the AARI measurements minimize the impacts of surface heterogeneities, 2) the key variable, ''cloud fraction,'' remains a somewhat controversial quantity in the Arctic cloud-radiation community (Rossow et al. 1993; Rossow 1995), and 3) the AARI values represent the MCRF, not the CRF used by other investigators. The results from the various sources, including the reanalyses, indicate that clouds warm the Arctic surface when integrated over the annual cycle. The reanalyses are less successful, however, in capturing the annual cycle of the effects of Arctic clouds.

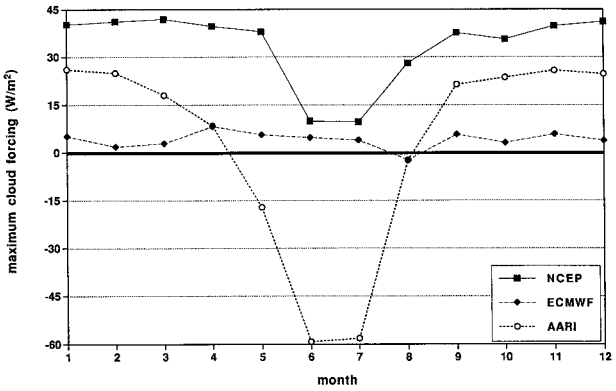

FIG. 19. Annual cycles of maximum cloud-radiative forcing (MCRF) from the NCEP reanalysis (solid squares), the ECMWF reanalysis (solid diamonds), and AARI ice station data (open circles).

4. Conclusions

The results show that the measured Arctic surface radiative fluxes are sensitive to cloudiness during both the short Arctic summer and the long Arctic winter. If defined on the basis of the cloud, radiation, and temperature climatologies, the Arctic winter lasts from November through March. During this ''season,'' the reported cloud fractions vary about a mean of 0.5–0.6, and an overcast warms the surface by 5°–10°C (relative to the clear-sky situation) through an enhancement of the downward longwave radiation. The warming by the radiative flux enhancement after a clear-to-cloudy transition has a 1–2-day timescale, while the cooling after a cloudy-to-clear transition has a timescale of about 12 h. The NCEP reanalysis exaggerates slightly the association between cloudiness and surface temperature, while the ECMWF reanalysis shows a considerably weaker association. These relative magnitudes of the cloud-temperature associations are consistent with the cloud-longwave forcing of the surface, as the NCEP downward longwave fluxes show a greater increase under cloudy skies than do the AARI measured values, while the ECMWF downward longwave fluxes show smaller increases than the AARI values. This consistency between the surface temperatures and downward

longwave fluxes may be fortuitous, however, because the temperatures are, to some extent, controlled by the observational data while the radiative fluxes are not.

The maximum cloud-radiative forcing, defined as the difference between the cloudy-sky and clear-sky net surface fluxes, is negative during May, June, and July because of the reduction of the downcoming solar flux by clouds. In this respect, the annual cycle of cloud radiative forcing in the AARI data is consistent with the ISCCP results, although the duration of the negative forcing is somewhat greater in the AARI and ISCCP results than in those of Curry and Ebert. As is the case with the actual cloud-radiative forcing deduced in earlier studies, the annual mean of the maximum cloud-radiative forcing derived from the AARI data is small but positive (approximately 3 W m^{-2}), implying that clouds reduce the net radiative loss of energy from Arctic surface, at least over the thick ice on which the AARI measurements were made. The effects of surface heterogeneities on this conclusion remain to be determined.

In the NCEP reanalysis, the annual mean of the maximum cloud-radiative forcing is also positive, but the negative forcing during the summer months is not captured by the reanalysis. This disagreement compounds the finding that the annual cycle of cloud coverage in the NCEP reanalyses disagrees considerably with the observed. The ECMWF reanalysis does not permit a meaningful assessment of the cloud-radiative forcing at this time because of the insensitivity of the ECMWF surface solar fluxes to the presence of clouds.

The dependence of the AARI cloud-radiative forcing on cloud fraction and month (Fig. 10) implies that a major decrease of June–July cloud fractions (that is, to values less than 0.5) would substantially increase the radiation reaching the Arctic surface. The annual mean of the cloud-radiative forcing would become more positive if such a change of cloudiness occurred, and changes in the underlying surface would undoubtedly introduce feedbacks into the system. An increase of cloudiness in the September–March period would also increase the radiation reaching the surface. Such inferences ignore possible changes in the cloud types and the cloud properties relevant to radiative interactions. The data collected during the SHEBA–ARM–FIRE field programs should enhance the prospects for including such factors, as well as the effects of surface heterogeneities, in a characterization of the Arctic surface radiative regime and its sensitivities. Algorithms derived from related remote sensing activities will be essential to the inclusion of surface heterogeneities. In the meantime, there is a need to address the Arctic cloud-radiative deficiencies in the reanalyses, since many of these deficiencies are likely common to the reanalyses and the GCMs used to simulate climate change. Until the seasonality and sign of the Arctic cloud-radiative forcing can be captured by the models used for the reanalyses, one must be cautious of model-derived projections of climate change in the Arctic.

Acknowledgments. This work was supported by the National Science Foundation, Climate Dynamics Program and Office of Polar Programs, through Grant ATM-9612324. The Russian ice station data were provided by the National Snow and Ice Data Center, while the NCEP reanalysis was obtained through the National Oceanic and Atmospheric Administration's Climate Diagnostics Center (http://www.cdc.noaa.gov). We thank Christian Jacob of ECMWF for helpful comments on the original manuscript and Norene McGhiey for the word processing of the manuscript.

REFERENCES

Curry, J. A., and E. E. Ebert, 1992: Annual cycle of radiation fluxes over the Arctic Ocean: Sensitivity to cloud optical properties. *J. Climate,* **5,** 1267–1280.

——, ——, and J. L. Schramm, 1993: Impact of clouds on the surface radiation balance of the Arctic Ocean. *Meteor. Atmos. Phys.,* **51,** 197–217.

——, W. B. Rossow, D. Randall, and J. L. Schramm, 1996: Overview of Arctic cloud and radiation characteristics. *J. Climate,* **9,** 1731–1764.

Gibson, J. K., P. Kallberg, S. Uppala, A. Hernandez, A. Nomura, and E. Serrano, 1997: *ECMWF Reanalysis, Project Rep. Series. Part 1. ERA Description.* European Centre for Medium-Range Weather Forecasts, 72 pp.

Hahn, C. J., S. G. Warren, and J. London, 1995: The effect of moonlight on observation of cloud cover at night and application to cloud climatology. *J. Climate,* **8,** 1429–1446.

Huschke, R. E., 1969: *Arctic Cloud Statistics from ''Air-Calibrated'' Surface Weather Observations.* The Rand Corporation, 79 pp.

IPCC, 1996: *Climate Change 1995: The Science of Climate Change.* Cambridge University Press, 572 pp.

Isaac, G. A., and R. A. Stuart, 1996: Relationships between cloud type and amount, precipitation, and surface temperature in the Mackenzie River Valley–Beaufort Sea area. *J. Climate,* **9,** 1921–1941.

Jacob, C., 1994: The impact of the new cloud scheme on ECMWF's integrated forecasting system (IFS). *Proc. ECMWF/GEWEX Workshop on Modelling, Validation and Assimilation of Clouds,* Reading, United Kingdom, ECWMF, 176–178.

Kalnay, E., and Coauthors, 1996: The NCEP/NCAR 40-year reanalysis project. *Bull. Amer. Meteor. Soc.,* **77,** 437–471.

Key, J. R., A. J. Schweiger, and R. S. Stone, 1997: Expected uncertainity in satellite-derived estimates of the surface radiation budget at high latitudes. *J. Geophys. Res.,* **102,** 15 837–15 847.

Kanimitsu, M., and Coauthors, 1991: Recent changes implemented into the global forecast system at NMC. *Wea. Forecasting,* **6,** 86–97.

Manabe, S., M. J. Spelman, and R. J. Stouffer, 1992: Transient response of a coupled ocean–atmosphere model to gradual changes of atmospheric CO_2. Part II: Seasonal response. *J. Climate,* **5,** 105–126.

Marshunova, M. S., and A. A. Mishin, 1994: *Handbook on the Radiation Regime of the Arctic Basin (from the Drifting Stations)* (English translation). Hydrometeorological Publishing House, St. Petersburg, Russia, 63 pp.

Martin, S., and E. A. Muñoz, 1997: Properties of the Arctic two-meter air temperature field for 1979 to the present derived from a new gridded dataset. *J. Climate,* **10,** 1428–1440.

Maykut, G. A., and P. E. Church, 1973: Radiation climate of Barrow, Alaska, 1962–66. *J. Appl. Meteor.,* **12,** 620–628.

Overland, J. E., and P. S. Guest, 1991: The Arctic snow and air temperature budget over sea ice during winter. *J. Geophys. Res.,* **96,** 4651–4662.

Perovich, D. K., and the SHEBA Phase II Science Team, 1997: SHE-

BA Implementation Plan, Draft Version 2.0., Rep. to National Science Foundation, Arlington, VA, 59 pp.

Randall, D. A., B. Albrecht, S. Cox, D. Johnson, P. Minnis, W. Rossow, and D. O'C. Starr, 1995: On FIRE at ten. *Advances in Geophysics,* Vol. 38, Academic Press, 37–177.

——, and Coauthors, 1998: Status of and outlook for large-scale modeling of atmosphere–ice–ocean interactions in the Arctic. *Bull. Amer. Meteor. Soc.*, **79,** 197–219.

Rossow, W. B., 1995: Another look at the seasonal variation of polar cloudiness with satellite and surface observations. Preprints, *Fourth Conf. on Polar Meteorology and Oceanography*, Dallas, TX, Amer. Meteor. Soc., J10 (1)–J10 (4).

——, and Y.-C. Zhang, 1995: Calculations of surface and top-of-atmosphere radiative fluxes from physical quantities based on ISCCP datasets. Part II. Validation and first results. *J. Geophys. Res.*, **100,** 1167–1197.

——, A. W. Walker, and L. C. Garder, 1993: Comparison of ISCCP and other cloud amounts. *J. Climate,* **6,** 2394–2418.

Schweiger, A. J., and J. R. Key, 1994: Arctic Ocean radiative fluxes and cloud forcing from the ISCCP C2 cloud dataset, 1983–1990. *J. Appl. Meteor.*, **33,** 948–963.

Serreze, M. C., J. A. Maslanik, and J. R. Key, 1997: Atmospheric and sea ice characteristics of the Arctic Ocean and the SHEBA field region in the Beaufort Sea. National Snow and Ice Data Center, Special Rep. 4, 219 pp.

Shine, K. P., 1984: Parameterization of shortwave flux over high albedo surfaces as a function of cloud thickness and surface albedo. *Quart. J. Roy. Meteor. Soc.*, **110,** 747–764.

Stamnes, K., R. G. Ellingson, J. A. Curry, J. E. Walsh, and B. D. Zak, 1999: Review of science issues, deployment strategy, and status for the ARM North Slope of Alaska/Adjacent Arctic Ocean (NSA/AAO) climate research site. *J. Climate,* in press.

Tao, X., J. E. Walsh, and W. L. Chapman, 1996: An assessment of global climate model simulations of Arctic air temperatures. *J. Climate,* **9,** 1060–1076.

Tiedtke, M., 1993: Representation of clouds in large-scale models. *Mon. Wea. Rev.*, **121,** 3040–3061.

Warren, S. G., C. J. Hahn, J. London, R. M. Chervin, and R. L. Jenne, 1988: Global distribution of total cloud cover and cloud type amounts over the Arctic Ocean. NCAR/TN-317+STR, 212 pp.

Zhang, T., K. Stamnes, and S. A. Bowling, 1996: Impact of clouds on surface rediative fluxes and snowmelt in the Arctic and subarctic. *J. Climate*, **9,** 2110–2123.